In-situ neutron imaging study of NH$_3$ absorption and desorption in SrCl$_2$ within a heat storage prototype reactor

Perizat Berdiyeva[a], Anastasiia Karabanova[b], Malgorzata G. Makowska[c], Rune E. Johnsen[b], Didier Blanchard[b], Bjørn C. Hauback[a], Stefano Deledda[a],*

[a] Department for Neutron Materials Characterization, Institute for Energy Technology, P.O. Box 40, NO-2027, Kjeller, Norway
[b] Department of Energy Conversion and Storage, Technical University of Denmark, Fysikvej, DK-2800, Lyngby, Denmark
[c] Photon Science Division, Paul-Scherrer Institute, Forschungsstrasse 111, 5232-Villigen, Switzerland

ABSTRACT

Strontium chloride octaammine Sr(NH$_3$)$_8$Cl$_2$ offers high volumetric and gravimetric NH$_3$ densities and can store and release heat upon exo-/endothermal absorption and desorption of NH$_3$. Thus, it is a promising material for thermochemical heat storage (THS) applications.

In the present work, *in-situ* neutron imaging was applied to analyze spatio-temporal development of Sr (NH$_3$)$_8$Cl$_2$ powder in a thermochemical heat storage prototype reactor during NH$_3$ absorption and desorption processes. The powder was embedded in a stainless steel honeycomb for the efficient heat transfer during the NH$_3$ desorption process. 2D radiography images were obtained during NH$_3$ ab-/desorption cycles at selected temperatures. The swelling and formation of the porous structure in SrCl$_2$ is monitored during the first cycles. A powder bed expansion of up to 10% upon NH$_3$ absorption was observed. Neutron tomography experiment were also performed to acquire 3D information which revealed the deformation of the honeycomb. This neutron imaging experiment brought crucial information for optimizing the design of efficient and safe THS systems.

1. Introduction

To support the transition from conventional fossil fuel energy sources to decarbonized sources, a number of technologies have been identified and are expected to have major impacts. The technologies range from renewable energy sources to efficient energy use, where the excess of energy can be first stored and later supplied to meet the demands. The effective use of energy requires efficient storage, which can be achieved using different methods one of them being thermal energy storage [1]. Seasonal heat storage materials such as hydrates [2] and ammines have been studied as thermochemical heat storage materials for domestic heating applications [3]. However, most hydrates were found to have poor cyclability and degrade over multiple cycles at temperature higher than 50 °C [4]. Meanwhile sorption metal chloride and ammonia working pairs are reported to have a very good cyclability and high energy density [5].

Metal ammines have for more than 15 years been studied as an indirect storage of hydrogen due to their high volumetric and gravimetric hydrogen capacities [6–8]. Sr(NH$_3$)$_8$Cl$_2$ is one of the best metal halide ammines for NH$_3$ storage due to its high hydrogen density [9] and high theoretical volumetric NH$_3$ density of 642 kg m^{-3} at RT [10].

It is obtained via absorption of NH$_3$ into SrCl$_2$. The absorption reaction is exothermic, while the endothermic desorption is achieved by applying heat. These exothermic and endothermic absorption and desorption reactions are associated with good kinetics and make the SrCl$_2$/Sr(NH$_3$)$_8$Cl$_2$ an interesting system for thermochemical heat storage (THS) applications [10,11]. In these applications, heat provided by an external source decomposes Sr(NH$_3$)$_8$Cl$_2$ into NH$_3$ gas and SrCl$_2$. The NH$_3$ gas can then be condensed into liquid NH$_3$ in a separate reservoir. In storage mode the connection between liquid NH$_3$ and SrCl$_2$ is closed. To recover the heat, NH$_3$ is transferred back to the container with SrCl$_2$, where heat is released upon the absorption process and formation of Sr (NH$_3$)$_8$Cl$_2$. By controlling the applied pressure of the NH$_3$ gas, the heat release can be controlled and varied. Ideally, the exothermal and endothermal absorption and desorption of NH$_3$ in SrCl$_2$ / Sr(NH$_3$)$_8$Cl$_2$ can be employed for handling waste heat (40–80 °C) from industry and be reused for district heating [1]. The SrCl$_2$/NH$_3$ working pair was selected due to its high energy density and very good cyclability. SrCl$_2$ is rather cheap and non-toxic. Its working temperature corresponds to the target application, i.e. residential heating, taking advantage of low-price renewable electricity (heat-pump + heat storage) and / or low-grade waste heat recovery (<100 °C) readily available at most

industrial production lines.

The crystal structures of $Sr(NH_3)_8Cl_2$, $SrCl_2$ and their intermediates have already been extensively studied and characterized [9,10]. However, the spatio-temporal evolution of the $Sr(NH_3)_8Cl_2$ and NH_3 transport in the system have not yet been investigated in detail. Neutrons are very well suited to determine the distribution of NH_3 molecules in the $SrCl_2/Sr(NH_3)_8Cl_2$ system due to their unique properties of "seeing" hydrogen atoms and to the high hydrogen content in this system.

Neutron imaging is a powerful characterization technique which can provide 2D and 3D information about the inner structure of objects [12]. It is used as a characterization method for various energy storage materials and systems. The strong interaction of neutrons with hydrogen makes neutrons an attractive probe within hydrogen storage, where neutron radiography and tomography techniques can be used not only for qualitative, but also quantitative studies [13–16]. Furthermore, energy storage devices such as fuel cells or batteries are studied extensively by neutron imaging. The sensitivity of neutrons to hydrogen in water molecules allows detecting and visualizing water distribution in fuel cells [17–20]. Neutrons are also sensitive to lithium, which is a key element in commercial rechargeable batteries [21–25]. Further details about neutron imaging techniques, its accuracy, sensitivity, and its applications in various fields of research can be found in several review papers published in the last decade [12,26,27].

In this work, NH_3 uptake and release in the $SrCl_2/Sr(NH_3)_8Cl_2$ system within a THS prototype reactor, was studied by neutron imaging. The specially designed THS prototype reactor contained $SrCl_2$ embedded in a stainless steel honeycomb structure. The designed THS reactor contains several honeycomb discs filled with $SrCl_2$ powder, which are placed on top of each other. In this work only the half of one whole disc was employed in order to examine the local NH_3 absorption and desorption. The honeycomb structure of the disc is used to provide an efficient heat transfer within the volume of the disc during the NH_3 desorption process, when heat is provided to the system. The high neutron scattering cross-section of hydrogen present in ammonia molecule allowed observation of the uptake and release of NH_3 within $SrCl_2$. Absorption and desorption profiles for different regions of the honeycomb were obtained for each absorption and desorption cycle by *in-situ* neutron radiography. The results of image analysis are discussed with respect to the homogeneity of the absorption and desorption processes over the volume of the THS reactor and how it is affected by the degree of the compaction of the powder, as well as how efficiently the stainless-steel honeycomb structure conducts the heat during NH_3 desorption.

To the best of our knowledge this is the first time that neutron imaging is used to characterize a THS reactor, allowing a real-time visualization of the changes that the sorption material undergoes during charging and discharging. The neutron radiography data presented here will be used to validate results from numerical simulations. A COMSOL Multiphysics modelling was developed for the heat reactor, integrating, with a high degree of accuracy, the thermochemistry, the ammonia flow, the heat transfer to optimize the reactor design and achieve high heat power and maximum use of the heat generated [28]. Neutron imaging will help, on one hand, to validate the simulation model, and, on the other hand, to validate or invalidate our first assumption on the honeycomb effect on heat transfer and diffusion to the salt.

2. Experimental

2.1. The THS reactor prototype set-up

A special transportable THS reactor prototype (118 mm in length, 20 mm in width and 85 mm in height) was designed for the neutron imaging experiment (Fig. 1). The THS reactor is made of 2 mm thick aluminum, in order to be as transparent as possible for neutrons to study the interior of the reactor. The THS reactor is tightly closed with a stainless-steel lid of 85 mm in diameter and an o-ring ensured the

sealing. The lid had two gas inlets (only one of them was used during this experiment) and a cylindrical inlet which housed a heating element and a thermocouple.

A honeycomb with the dimensions of $100 \times 50 \times 10$ mm was filled with 10 g of $SrCl_2$ salt and placed inside the THS reactor in an inert argon gas filled glove box (< 1 ppm of O_2 and H_2O). Two absorption and desorption cycles were performed on the $SrCl_2$ prior to the neutron imaging experiment in order to confirm the cyclability and suitability of the sample. The THS reactor was then connected through a stainless-steel tube to a reservoir, which contained 100 g of $Sr(NH_3)_8Cl_2$ powder that served as NH_3 source and reservoir during the experiment. Manual valves and a pressure reader (Fig. 2) were included in the connection between the THS reactor and the reservoir. The reservoir and the prototype reactor were connected to a heating element and a thermocouple for controlling and monitoring the temperature.

The $Sr(NH_3)_8Cl_2$ in the reservoir was heated up to 70 °C during the experiment which then released NH_3 gas that was absorbed by the $SrCl_2$ salt in the honeycomb at RT. Upon heating the honeycomb in the THS reactor, NH_3 was released from the $Sr(NH_3)_8Cl_2$ powder and reabsorbed in the reservoir. The pressure of the system was remotely monitored and logged.

2.2. Neutron imaging set-up

The neutron radiography and tomography experiments were performed at the NECTAR instrument, at the FRM-II research reactor in Garching, Germany using a white beam of thermal neutrons (mean energy 28 meV) [29]. The sample was mounted on a stage allowing translation along *x, y* and *z*-axes about 3 cm in case of radiography and about 10 cm for tomography from the scintillator screen. The thermal neutron beam transmitted through the sample impinged on a scintillator screen $ZnS/^6LiF$, which converted the neutrons into light. The light was then reflected by a mirror in a light-tight box and captured by CCD camera (Andor iKon-L-BV) with a 2048 × 2048 pixels resolution. The experiment did not require high spatial resolution, thus the collimation ratio L/D, which was about 230, provided sufficient image quality. Prior to each experiment open beam and dark current images were collected for normalization of the raw images using ImageJ [30]. The total acquisition time for each image including camera readout was 27 s and overall three absorption and two desorption processes were performed. Each absorption step, except the last one, was followed by desorption allowing us to investigate not only the absorption and desorption processes themselves, but also the difference between the first and next cycles. The honeycomb with $SrCl_2$ powder was open in the front side for free NH_3 and $SrCl_2$ powder interaction.
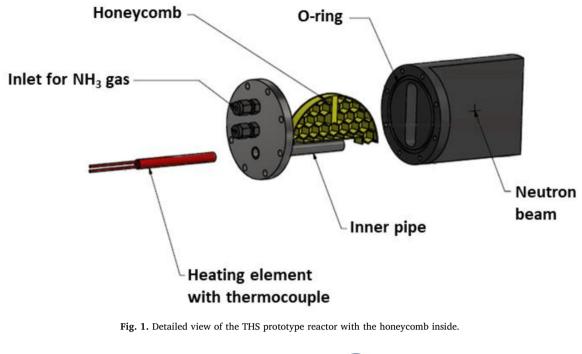
Neutron tomography measurements were carried out by placing the THS reactor in a vertical position and by rotating it over a 360° range. During the tomography experiment the THS reactor was disconnected from the reservoir. Several tomography scans, each with 1083 projections, were performed for different degrees of saturation of NH_3 in $Sr(NH_3)_8Cl_2$ and then 3D volume of the sample was reconstructed using MuhRec software [31] and visualized using Tomviz software [32].

The formation of $Sr(NH_3)_8Cl_2$, thus NH_3 concentration in the sample was defined by the normalized transmission $I(\lambda)$ (greyscale values between 0 and 1) in selected areas of the images, where I is the normalized intensity and λ is the neutron wavelength. The lower transmission $I(\lambda)$ represents the higher concentration of NH_3 while the higher transmission $I(\lambda)$ means lower NH_3 content in the sample.

3. Results and discussion

3.1. Absorption process

In-situ transmission images were obtained during NH_3 absorption and desorption processes in the $SrCl_2$ powder. The series of images in Fig. 3 show the honeycomb at the end of absorption-1 (a), absorption-2
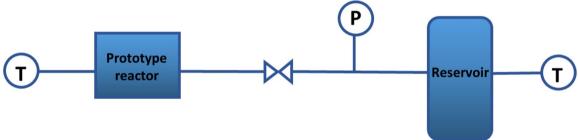
Fig. 1. Detailed view of the THS prototype reactor with the honeycomb inside.

Fig. 2. Schematic view of the setup used for the neutron imaging experiment. The letters P and T indicate the points where pressure and temperature were measured.

(b) and absorption-3 (c). These images were obtained by normalization of corresponding images by the image of the sample in the initial state. Therefore, the images show only the changes that occurred in the sample due to NH_3 absorption. The formation of $Sr(NH_3)_8Cl_2$ appears as dark areas during NH_3 uptake due to the high neutron attenuation of hydrogen atoms [19] contained in ammonia molecules.

The different transmission $I(\lambda)$ at the end of each NH_3 absorption process suggests a different extent of NH_3 uptake (see Fig. 3). Transmission values $I(\lambda)$ were obtained by marking a hexagonal area in one cell of the honeycomb (cell-1, Fig. 4a) and calculating the mean value over the selected area. Fig. 4a presents the mean $I(\lambda)$ change over time in this cell. The graph shows a clear difference in transmission between the absorption-1, absorption-2 and absorption-3. During absorption-3, a

lower greyscale value of 0.357 was reached compared to the absorption-1 and absorption-2, where the greyscale values were 0.622 and 0.551 at the end of absorption, respectively. This is the result of powder expansion during the NH_3 absorption processes and formation of macroporous structure [9], which creates paths for more NH_3 to diffuse into the powder bed during the following absorption processes. For this reason, absorption-2 and absorption-3 resulted in more ammoniated areas in the radiography images than those observed in absorption-1 (Fig. 3). However, as seen in Fig. 4, the change in the transmission $I(\lambda)$ with time, for a given absorption, does not stabilize to minimal values suggesting that the absorption processes were not completed.

The pressure in the system was monitored during the NH_3 absorption (see Fig. 4b). As the reservoir was heated and NH_3 was released
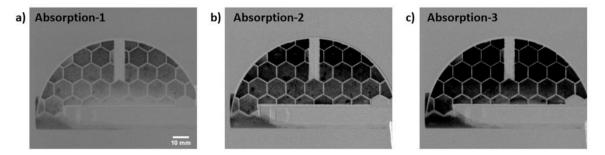

Fig. 3. Neutron radiography images. The series of normalized images representing the sample after each absorption process (**a**) absorption-1, (**b**) absorption-2 and (**c**) absorption-3.
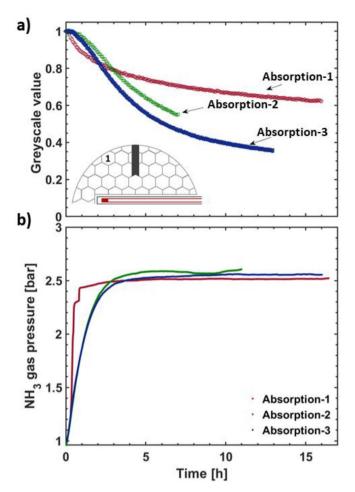
Fig. 4. NH_3 gas absorption in $SrCl_2$ contained in the THS reactor. (**a**) the change in transmission $I(\lambda)$ in the cell-1 and (**b**) NH_3 gas pressure during the absorption processes.
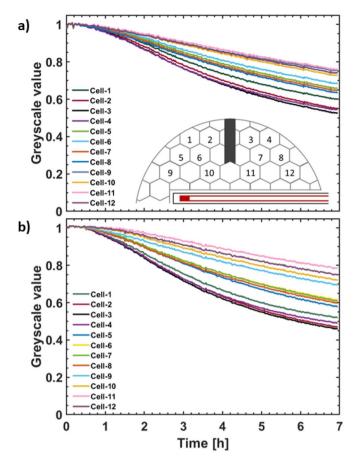

Fig. 5. The change in transmission $I(\lambda)$ through the powder during (**a**) absorption-2 and (**b**) absorption-3. The schematic view of the honeycomb with selected and numbered cells is included in graph a.

from the $Sr(NH_3)_8Cl_2$ salt in the reservoir, the pressure of the system increased to 2.5 bar, which is the equilibrium pressure of $Sr(NH_3)_8Cl_2$ at 70 °C. Once the NH_3 absorption process started in the THS reactor, the pressure was stabilized due to the equal rate of NH_3 release from $Sr(NH_3)_8Cl_2$ in the reservoir and the NH_3 absorption by $SrCl_2$ in the THS honeycomb structure.

A more detailed analysis of the $Sr(NH_3)_8Cl_2$ formation during absorption-2 and absorption-3 was performed on selected cells of the honeycomb. Mean transmission values $I(\lambda)$ were calculated by averaging over the area of the selected cells during the first 7 h of absorption. The results are plotted in Fig. 5 for absorption-2 (a) and absorption-3 (b), respectively. It can be observed that the formation of $Sr(NH_3)_8Cl_2$ is inhomogeneous over the honeycomb volume. The NH_3 distribution in the different cells of the honeycomb differs depending on their position within the honeycomb. Fig. 5a shows that the topmost cells have the lowest mean greyscale value (higher concentration of NH_3) between 0.603 and 0.528 (cell-1, -2, -3 and -4) whereas the cells in the bottom (cell-9, -10, -11 and -12) have higher mean greyscale values (lower concentration of NH_3) between 0.756 and 0.744. The same trend can be seen during the third absorption process (Fig. 5b). The lowest mean greyscale value calculated was 0.459 in the cell-3, whereas the highest value was 0.783 in the cell-11. Cell-5, -6, -7 and -8 located in the middle of the honeycomb show intermediate mean greyscale value between 0.579 and 0.613, which means that the NH_3 concentration in those cells is the intermediate between the NH_3 concentration in the top and bottom cells.

Several reasons might contribute to these results. Firstly, it should

be noted that the NH_3 gas inlet was placed at the top right of the THS reactor, letting the powder particles on top cells absorb NH_3 gas earlier than the powder contained in the lower cells. Secondly, the free space between the THS reactor inner walls and the honeycomb allowed some powder to fall out of the honeycomb. Therefore, the powder thickness over the honeycomb was inhomogeneous, providing different amount of $SrCl_2$ salt in the different cells of the honeycomb and resulting in different NH_3 concentration. Finally, the honeycomb with the salt was prepared in an inert argon atmosphere, which filled the THS reactor prior to the start of the experiment. The THS reactor was not evacuated before the first NH_3 absorption process, so Ar gas was still present inside the reactor during absorption. The different densities of Ar and NH_3 gases, 1.661 kg/m^3 and 0.717 kg/m^3 at RT, respectively, might have created layers of NH_3 gas on the top and Ar on the bottom, preventing a homogeneous NH_3 gas flow towards the bottom of the THS reactor.

The expansion of $Sr(NH_3)_8Cl_2$ over time during the NH_3 uptake was studied by placing the honeycomb horizontally so that powder thickness change is perpendicular to the neutron beam. Side-view images were obtained while performing a NH_3 absorption process. The volume expansion of the $Sr(NH_3)_8Cl_2$ powder within the honeycomb is shown in Fig. 6. The expansion of the $Sr(NH_3)_8Cl_2$ in axial direction with time can be observed. The packing within the honeycomb prevented the $Sr(NH_3)_8Cl_2$ powder from expanding in the radial direction, while free space between the honeycomb and THS reactor wall allowed the axial expansion. During this process NH_3 absorption over time produced a gradual expansion of the salt by up to 10% in height.
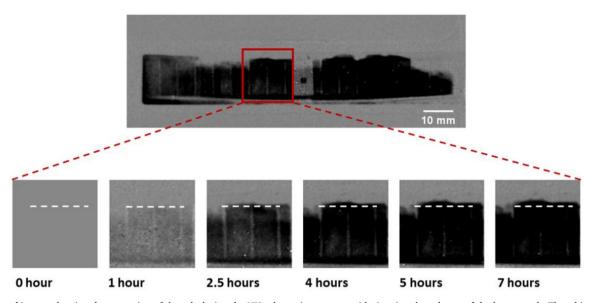
Fig. 6. Series of images showing the expansion of the salt during the NH_3 absorption process with time in selected area of the honeycomb. The white dashed line shows the initial height of the powder. (Full-size image above the series was acquired at the 4th hour of absorption-4).

3.2. Desorption process

Neutron radiography was carried out on the THS reactor during the desorption processes at selected temperatures. The two desorption processes were performed at 220 °C and 100 °C at 1 bar of ammonia pressure, and full release of NH_3 was observed after 46 min and 3 h 45 min, respectively. During desorption at 220 °C $Sr(NH_3)_8Cl_2$ was decomposed into $SrCl_2$ and NH_3, while at 100 °C the end products were $Sr(NH_3)Cl_2$ and NH_3. This is due to two-step desorption occurring in $Sr(NH_3)_8Cl_2$ at the given temperatures and ammonia pressure of 1 bar [6,9,10].

Fig. 7a and b show the change in transmission $I(\lambda)$ in the cell-1 and the pressure profile of the system during desorption processes. At 220 °C, the pressure increased drastically because of the large amount of NH_3 gas released in a short time and started decreasing after few minutes as NH_3 is absorbed in the reservoir. Fig. 7c and d show the transmission images of the honeycomb 20 min after the start of the desorption processes. The decomposition of $SrCl_2(NH_3)_8$ into $SrCl_2$ and NH_3 is almost complete after 20 min at 220 °C. The powder in the cells closer to the heat source desorbed NH_3 faster than the powder in cells further away from the heating source. It should be mentioned that the special stainless-steel honeycomb was prepared to provide a higher heat transfer. The hexagon-shaped cells should provide efficient heat transmission from cell to cell and thus improving the NH_3 desorption efficiency of the whole plate. The images in Fig. 7 show that heat conductivity of the stainless-steel was not sufficient for ensuring homogeneous NH_3 release. The NH_3 desorption process within all 12 cells was analyzed and included in the supplementary information (Fig. A.1).

In order to observe the NH_3 release in detail, selected cells of the honeycomb were analyzed. The rate of desorption in each cell volume was studied by drawing lines parallel to the hexagon edges and measuring the transmission $I(\lambda)$ integrated along those lines and plotted as a function of time (see Fig. 8). The lines are at distance of 2 mm from each edge of the hexagon. The NH_3 gas release over time at the sides of the cells gives us information about the heat efficiency of the total stainless-steel net since NH_3 release takes place only when $Sr(NH_3)_8Cl_2$ salt is heated.

Fig. 8a shows a schematic view of the honeycomb and three cells selected for investigation of the change of NH_3 concentration during the desorption process at 100 °C. Fig. 8b, c and d illustrate the drop of NH_3 content along the lines in the cell-2, 6 and 10, respectively.

In all three cells we see that the release of NH_3 is not uniform, and it changes according to the heat direction. The transmission through the absorbed NH_3 along the lines also strongly depends on the position of the analyzed area with respect to the relative distance from the heating element. The bottom-right edges, i.e. closer to the heat source (B, C and D) are those where NH_3 is released earlier, indicating that they are the first to be heated. On the other hand, the top-left ones (A, E and F) are those where NH_3 is released later, pointing out they are heated later. Overall, the desorption of NH_3 from powder in the top parts of one cell happens mainly because of the heat is transferred through the salt inside the cell rather than from the cell walls. Besides, full NH_3 release happened within 1.5 h in cell-10, which is the closest to the heating element, whereas NH_3 desorption was completed after about 3 and 3.5 h in cell-6 and cell-2, the furthest from the heat source, respectively. The different time for NH_3 release in different areas of the honeycomb indicates that the stainless steel is not an ideal material for the efficient heat transfer, as the desorption process is inhomogeneous both along the honeycomb and within each cell. Similar calculations for other cells were performed and are included as supplementary information (Fig. A.2).

3.3. Neutron tomography

Ex-situ tomography studies were performed on the THS reactor, which was disconnected from the reservoir and placed vertically in front of the neutron beam. 3D images of the THS reactor after one absorption and desorption cycle (Fig. 9a), after NH_3 absorption (Fig. 9b) and after partial NH_3 desorption (Fig. 9c) were obtained and visualized. A clear contrast between $Sr(NH_3)_8Cl_2$ and $SrCl_2$ can be observed. To visualize the partially desorbed state of the salt a desorption process during *in-situ* neutron radiography measurements was terminated after 30 min and the scan over 360° was performed on the sample.

In all 3D visualizations sample powders outside the honeycomb can be noticed. This was also observed in the series of images acquired during absorption and shown in the Fig. 3. The sample thickness irregularity in the honeycomb cells confirms that the powder was initially inside the cells. Each radiography/tomography switch during the experiments required the movement of the THS reactor from horizontal to vertical positions causing loose powder to fall from the honeycomb and movement of the honeycomb itself loosing contact with the heating element.
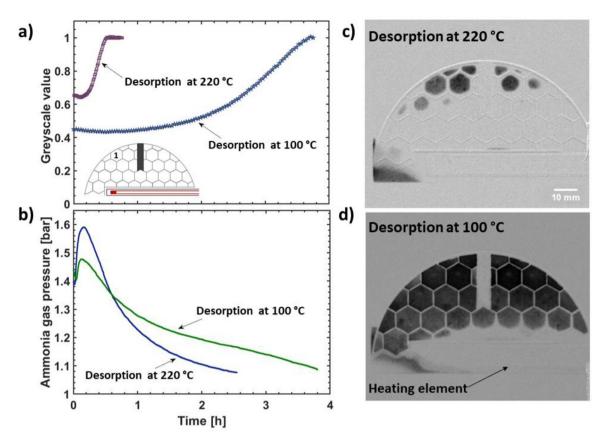
Fig. 7. The desorption processes of $SrCl_2(NH_3)_8$ at 220 °C and 100 °C: **(a)** changes of the transmission $I(\lambda)$ and **(b)** corresponding pressure profile. Transmission images obtained after 20 min of NH_3 desorption processes performed at **(c)** 220 °C and **(d)** 100 °C.

$Sr(NH_3)_8Cl_2$ in the Fig. 9b shows that the powder occupies a slightly bigger volume in the cells compared to $SrCl_2$ (a), due to the $SrCl_2$ powder expansion during NH_3 absorption and shrinkage after NH_3 desorption. The 3D visualization of the partially desorbed state in Fig. 9c confirms the direction of the desorption reaction discussed above (Fig. 8) and that the $Sr(NH_3)_8Cl_2$ powder in the cells close to the heating element started releasing NH_3 first.

The 3D visualization of the $Sr(NH_3)_8Cl_2$ in Fig. 9b was further analyzed by cutting orthogonal slices and studying the reactor in different planes. This allowed for a detailed view "inside" the investigated sample. This is shown in Fig. 10, which displays the $Sr(NH_3)_8Cl_2$ powder in the honeycomb viewed through the XY and YZ-planes. The powder separated by the cell walls can be recognized and the irregular height of the powder both within each cell and over the honeycomb is confirmed. Additionally, a significant deformation of the honeycomb is observed by viewing the sample through two different planes.

In Fig. 10 the red dashed line represents the original position of the honeycomb back plate, being flat before the experiments, but is found bended after the NH_3 absorption. This is likely caused by the $SrCl_2$ expansion occurring during NH_3 absorption and formation of $Sr(NH_3)_8Cl_2$. The stainless steel cell walls kept the powder from expanding in the radial direction, while the open front of the honeycomb allowed the powder to expand in the axial direction as displayed in Fig. 6. This volume expansion caused stresses on the honeycomb back plate pushing it away from the honeycomb net. It should be noted that the back plate was welded to the honeycomb only along outer edges, but not to the entire net, making it vulnerable to potential stresses.

3.4. Feasibility of quantitative analysis of the acquired neutron imaging data

This work was focused only on the qualitative analysis of the

obtained neutron imaging data. While it is generally possible to perform quantitative analysis from neutron imaging data, several uncertainties prevented us from quantifying in a reliable manner the NH_3 content in the investigated sample. In principle, the NH_3 content in the powder can be calculated from the neutron attenuation coefficient of NH_3. When neutrons pass through the sample, they are attenuated according the Beer-Lambert's law:

$$I(\lambda) = I_0 e^{-\mu(\lambda)x}$$

where I is an attenuated beam intensity, I_0 is an intensity behind a sample, μ is the neutron attenuation coefficient, λ is the neutron wavelength and x is the thickness of the sample. Here the dependence on neutron wavelength is neglected since the variation of the neutron attenuation coefficient of NH_3 and $SrCl_2$ for the herein used thermal spectrum does not affect the presented qualitative results. For a precise quantitative analysis, it would be proper to use monochromatic beam, which on the other hand would result in worse time resolution. Thus, for the presented experiment, using whole available spectrum was advantageous. The small sample thickness allows to neglect the beam hardening effect [33].

As seen from the 2D and 3D images, some amount of powder fell off the honeycomb causing irregularities in the powder thickness over the volume. The honeycomb was open on one side for facilitating the interaction between NH_3 and $SrCl_2$. This allowed for some of the $SrCl_2$ to be displaced outside the honeycomb while mounting the reactor on the sample stage. As a result, the initial thickness of the powder in the honeycomb changed and could not be determined accurately for further calculation of the NH_3 wt.%.

Finally, it should also be noted that the incoherent scattering from hydrogen contained in the NH_3 molecule results in additional errors. In particular, incoherent scattering causes the transmission behind the sample values to appear higher than the real values [34]. This can lead
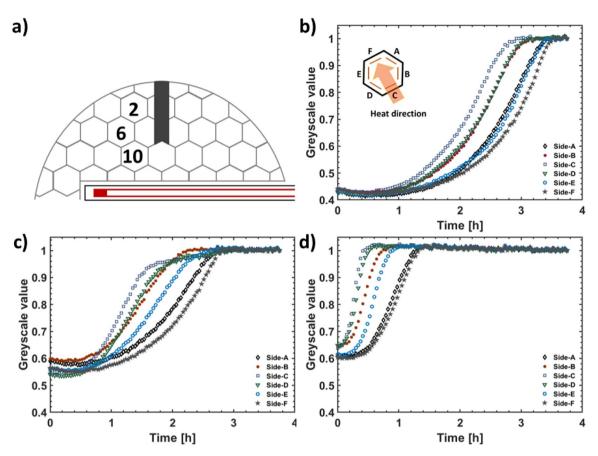
Fig. 8. The change of transmission I(λ) integrated along the selected volumes of the powder during desorption process at 100 °C (**a**) a schematic view of the honeycomb with the selected cells and the changes in transmission I(λ) along the lines drawn in cell-2 (**b**), cell-6 (**c**) and cell-10 (**d**). The heat direction is shown in the graph and is approximately the same in all three cases (**b**).

to underestimate the thickness of the volume occupied by NH_3 and, in turn, the NH_3 concentration. A method for improving the quantification of neutron imaging measurements with scintillator-camera based detectors by correcting for biases introduced by scattered neutrons using reference measurement with a grid of neutron absorbers called black bodies (BB) was developed [35–37]. However, this method was not applied during the neutron imaging experiment discussed in this work.

4. Summary

Neutron imaging is an excellent method for evaluating NH_3 distribution in the $SrCl_2/Sr(NH_3)_8Cl_2$ system. It offers a unique possibility

to study simultaneously NH_3 spatial distribution and the structural changes in the sample such as volume expansion of the powder during NH_3 absorption, which in turn might produce mechanical stresses on the THS reactor. In this work, we showed the inhomogeneous formation of $Sr(NH_3)_8Cl_2$ during NH_3 absorption processes which was possibly due to the location of the NH_3 gas inlet in the reactor and the presence of Ar in the cell at the beginning of the experiment. The latter remained at the bottom of the cell preventing NH_3 absorption in some parts of the powder. It was also shown that the stainless-steel honeycomb structure was not efficient for transferring the heat from the heating element to the edges of the honeycomb during the NH_3 desorption processes, as slower desorption kinetics are observed in the regions farthest away
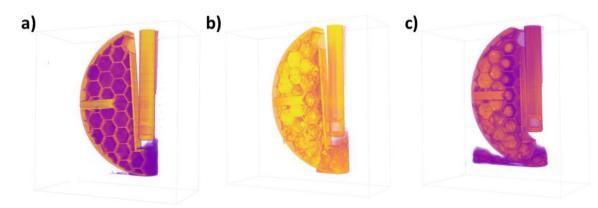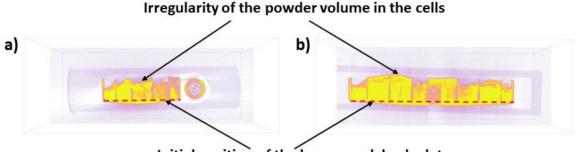

Fig. 9. 3D visualization of the honeycomb created with Tomviz software (**a**) fully desorbed $SrCl_2$ salt, (**b**) $Sr(NH_3)_8Cl_2$ and (**c**) the salt with partially desorbed NH_3. The colors of the different states are arbitrary and represented by the transmission through the absorbed NH_3 intensities.

Fig. 10. Deformation of the honeycomb back plate after the NH_3 absorption process (**a**) XY-plane, slice $z = 394$ and (**b**) YZ-plane, slice $x = 310$. The red dashed lines represent the position of the back plate before the absorption process.

from the heater. Additional investigations by neutron tomography showed that the back plate supporting the honeycomb structure was deformed after the volume expansion during NH_3 absorption in the powder.

The results presented here demonstrate that neutron imaging techniques are ideal and powerful tools for investigating thermochemical heat storage prototype systems and provided critical information on $SrCl_2$ powder behavior upon NH_3 absorption and desorption reactions. Based on these results, some improvements – e.g. a honeycomb disc made of a material with better heat conductivity than stainless steel – will be implemented and tested. The outcome of those tests will be crucial for designing a safe and efficient THS reactor.

CRediT authorship contribution statement

Perizat Berdiyeva: Formal analysis, Investigation, Data curation, Visualization, Writing - original draft. **Anastasiia Karabanova:** Methodology, Formal analysis, Investigation, Resources, Writing - review & editing. **Malgorzata G. Makowska:** Formal analysis, Investigation, Writing - review & editing. **Rune E. Johnsen:** Conceptualization, Methodology, Investigation, Writing - review & editing. **Didier Blanchard:** Conceptualization, Methodology, Investigation, Resources, Project administration, Writing - review & editing, Funding acquisition. **Bjørn C. Hauback:** Writing - review & editing, Supervision. **Stefano Deledda:** Conceptualization, Investigation, Resources, Writing - review & editing, Supervision, Funding acquisition.

Declaration of Competing Interest

X The authors declare that they have no known competing financial interests or personal relationships that could have appeared to influence the work reported in this paper.

Acknowledgements

Supplementary materials

Supplementary material associated with this article can be found, in the online version, at doi:10.1016/j.est.2020.101388.

References

[1] D. Aydin, S.P. Casey, S. Riffat, The latest advancements on thermochemical heat storage systems, Renew. Sustain. Energy Rev. 41 (2015) 356–367, https://doi.org/10.1016/j.rser.2014.08.054.

[2] P.A.J. Donkers, L.C. Sogutoglu, H.P. Huinink, H.R. Fischer, O.C.G. Adan, A review of salt hydrates for seasonal heat storage in domestic applications, Appl. Energy 199 (2017) 45–68, https://doi.org/10.1016/j.apenergy.2017.04.080.

[3] H. Jarimi, D. Aydin, Z. Yanan, G. Ozankaya, X. Chen, S. Riffat, Review on the recent progress of thermochemical materials and processes for solar thermal energy storage and industrial waste heat recovery, Int. J. Low-Carbon Technol. 14 (2019) 44–69, https://doi.org/10.1093/ijlct/cty052.

[4] L.C. Sogutoglu, P.A.J. Donkers, H.R. Fischer, H.P. Huinink, O.C.G. Adan, In-depth investigation of thermochemical performance in a heat battery: cyclic analysis of K_2CO_3, $MgCl_2$ and Na_2S, Appl. Energy 215 (2018) 159–173, https://doi.org/10.1016/j.apenergy.2018.01.083.

[5] T. Yan, Z.H. Kuai, S.F. Wu, Experimental investigation on a $MnCl_2$–$SrCl_2$/NH_3 thermochemical resorption heat storage system, Renew. Energy 147 (2020) 874–883, https://doi.org/10.1016/j.renene.2019.09.033.

[6] T. Vegge, R.Z. Sørensen, A. Klerke, J.S. Hummelshøj, T. Johannessen, J.K. Nørskov, C.H. Christensen, 19 - Indirect hydrogen storage in metal ammines, in: G. Walker (Ed.), Solid-State Hydrog. Storage, Woodhead Publishing, 2008, pp. 533–564, , https://doi.org/10.1533/9781845694944.4.533.

[7] C.H. Christensen, R.Z. Sørensen, T. Johannessen, U.J. Quaade, K. Honkala, T.D. Elmøe, R. Køhler, J.K. Nørskov, Metal ammine complexes for hydrogen storage, J. Mater. Chem. 15 (2005) 4106–4108, https://doi.org/10.1039/B511589B.

[8] A. Klerke, C.H. Christensen, J.K. Nørskov, T. Vegge, Ammonia for hydrogen storage: challenges and opportunities, J. Mater. Chem. 18 (2008) 2304–2310, https://doi.org/10.1039/B720020J.

[9] S. Lysgaard, A.L. Ammitzbøll, R.E. Johnsen, P. Norby, U.J. Quaade, T. Vegge, Resolving the stability and structure of strontium chloride amines from equilibrium pressures, XRD and DFT, Int. J. Hydrog. Energy 37 (2012) 18927–18936, https://doi.org/10.1016/j.ijhydene.2012.09.129.

[10] R.E. Johnsen, P.B. Jensen, P. Norby, T. Vegge, Temperature- and pressure-induced changes in the crystal structure of $Sr(NH_3)8Cl_2$, J. Phys. Chem. C. 118 (2014) 24349–24356, https://doi.org/10.1021/jp508076c.

[11] A. Bialy, P.B. Jensen, D. Blanchard, T. Vegge, U.J. Quaade, Solid solution barium–strontium chlorides with tunable ammonia desorption properties and superior storage capacity, J. Solid State Chem. 221 (2015) 32–36, https://doi.org/10.1016/j.jssc.2014.09.014.

[12] M. Strobl, I. Manke, N. Kardjilov, A. Hilger, M. Dawson, J. Banhart, Advances in neutron radiography and tomography, J. Phys. Appl. Phys. 42 (2009) 243001, , https://doi.org/10.1088/0022-3727/42/24/243001.

[13] A. Baruj, M. Ardito, J. Marín, F. Sánchez, E.M. Borzone, G. Meyer, Design and characterization of a hydride-based hydrogen storage container for neutron imaging studies, Phys. Procedia 69 (2015) 491–495, https://doi.org/10.1016/j.phpro.2015.07.069.

[14] Ł. Gondek, N.B. Selvaraj, J. Czub, H. Figiel, D. Chapelle, N. Kardjilov, A. Hilger, I. Manke, Imaging of an operating LaNi$_4$.8Al0.2–based hydrogen storage container, Int. J. Hydrog. Energy. 36 (2011) 9751–9757, https://doi.org/10.1016/j.ijhydene.2011.05.089.

[15] F. Heubner, A. Hilger, N. Kardjilov, I. Manke, B. Kieback, Ł. Gondek, J. Banhart, L. Röntzsch, In-operando stress measurement and neutron imaging of metal hydride composites for solid-state hydrogen storage, J. Power Sources 397 (2018) 262–270, https://doi.org/10.1016/j.jpowsour.2018.06.093.

[16] M.G. Makowska, L.T. Kuhn, H.L. Frandsen, E.M. Lauridsen, S. De Angelis, L.N. Cleemann, M. Morgano, P. Trtik, M. Strobl, Coupling between creep and redox behavior in nickel - yttria stabilized zirconia observed in-situ by monochromatic neutron imaging, J. Power Sources 340 (2017) 167–175, https://doi.org/10.1016/j.jpowsour.2016.11.059.

[17] P. Boillat, E.H. Lehmann, P. Trtik, M. Cochet, Neutron imaging of fuel cells – recent trends and future prospects, Curr. Opin. Electrochem. 5 (2017) 3–10, https://doi.org/10.1016/j.coelec.2017.07.012.

[18] J. Zhang, D. Kramer, R. Shimoi, Y. Ono, E. Lehmann, A. Wokaun, K. Shinohara, G.G. Scherer, In situ diagnostic of two-phase flow phenomena in polymer

electrolyte fuel cells by neutron imaging: Part B. material variations, Electrochim. Acta 51 (2006) 2715–2727, https://doi.org/10.1016/j.electacta.2005.08.010.

[19] M. Siegwart, R.P. Harti, V. Manzi-Orezzoli, J. Valsecchi, M. Strobl, C. Grünzweig, T.J. Schmidt, P. Boillat, Selective visualization of water in fuel cell gas diffusion layers with neutron dark-field imaging, J. Electrochem. Soc. 166 (2019) F149–F157, https://doi.org/10.1149/2.1011902jes.

[20] D.S. Hussey, D.L. Jacobson, M. Arif, K.J. Coakley, D.F. Vecchia, In situ fuel cell water metrology at the NIST neutron imaging facility, J. Fuel Cell Sci. Technol. (2010) 7, https://doi.org/10.1115/1.3007898.

[21] I. Manke, H. Markötter, C. Tötzke, N. Kardjilov, R. Grothausmann, M. Dawson, C. Hartnig, S. Haas, D. Thomas, A. Hoell, C. Genzel, J. Banhart, Investigation of energy-relevant materials with synchrotron x-rays and neutrons, Adv. Eng. Mater. 13 (2011) 712–729, https://doi.org/10.1002/adem.201000284.

[22] A. Senyshyn, M.J. Mühlbauer, K. Nikolowski, T. Pirling, H. Ehrenberg, "In-operando" neutron scattering studies on Li-ion batteries, J. Power Sources 203 (2012) 126–129, https://doi.org/10.1016/j.jpowsour.2011.12.007.

[23] G.V. Riley, D.S. Hussey, D. Jacobson, In situ neutron imaging of alkaline and lithium batteries, ECS Trans. 25 (2010) 75–83, https://doi.org/10.1149/1.3414005.

[24] Z. Nie, P. McCormack, H.Z. Bilheux, J.C. Bilheux, J.P. Robinson, J. Nanda, G.M. Koenig, Probing lithiation and delithiation of thick sintered lithium-ion battery electrodes with neutron imaging, J. Power Sources 419 (2019) 127–136, https://doi.org/10.1016/j.jpowsour.2019.02.075.

[25] K. Kino, M. Yonemura, Y. Kiyanagi, Y. Ishikawa, Joseph.Don. Parker, T. Tanimori, T. Kamiyama, First imaging experiment of a lithium ion battery by a pulsed neutron beam at J-PARC/MLF/BL09, Phys. Procedia. 69 (2015) 612–618, https://doi.org/10.1016/j.phpro.2015.07.087.

[26] N. Kardjilov, I. Manke, A. Hilger, M. Strobl, J. Banhart, Neutron imaging in materials science, Mater. Today 14 (2011) 248–256, https://doi.org/10.1016/S1369-7021(11)70139-0.

[27] N. Kardjilov, I. Manke, R. Woracek, A. Hilger, J. Banhart, Advances in neutron imaging, Mater. Today 21 (2018) 652–672, https://doi.org/10.1016/j.mattod.2018.03.001.

[28] S.N. Gunasekara, M. Laios, A. Karabanova, V. Martin, D. Blanchard, Numerical Design of a Reactor-Heat Exchanger Combined Unit for Ammonia-SrCl2 Thermochemical Storage System, (2019), pp. 1–12.

[29] T. Bücherl, S. Söllradl, NECTAR: radiography and tomography station using fission neutrons, J. Large-Scale Res. Facil. 1 (2015) 19, https://doi.org/10.17815/jlsrf-1-45.

[30] ImageJ2: ImageJ for the next generation of scientific image data | BMC Bioinformatics | Full Text, (n.d.). https://bmcbioinformatics.biomedcentral.com/articles/10.1186/s12859-017-1934-z(accessed October 23, 2019).

[31] A.P. Kaestner, MuhRec—a new tomography reconstructor, Nucl. Instrum. Methods Phys. Res. Sect. 651 (2011) 156–160, https://doi.org/10.1016/j.nima.2011.01.129.

[32] M.D. Hanwell, C.J. Harris, A. Genova, J. Schwartz, Y. Jiang, R. Hovden, Tomviz: open source platform connecting image processing pipelines to GPU accelerated 3D visualization, Microsc. Microanal. 25 (2019) 408–409, https://doi.org/10.1017/S1431927619002770.

[33] E.H. Lehmann, P. Vontobel, N. Kardjilov, Hydrogen distribution measurements by neutrons, Appl. Radiat. Isot. 61 (2004) 503–509, https://doi.org/10.1016/j.apradiso.2004.03.075.

[34] R. Hassanein, F. de Beer, N. Kardjilov, E. Lehmann, Scattering correction algorithm for neutron radiography and tomography tested at facilities with different beam characteristics, Phys. B Condens. Matter. 385–386 (2006) 1194–1196, https://doi.org/10.1016/j.physb.2006.05.406.

[35] P. Boillat, C. Carminati, F. Schmid, C. Grünzweig, J. Hovind, A. Kaestner, D. Mannes, M. Morgano, M. Siegwart, P. Trtik, P. Vontobel, E.H. Lehmann, Chasing quantitative biases in neutron imaging with scintillator-camera detectors: a practical method with black body grids, Opt. Express. 26 (2018) 15769–15784, https://doi.org/10.1364/OE.26.015769.

[36] P. Trtik, E.H. Lehmann, Progress in high-resolution neutron imaging at the Paul Scherrer Institut - the neutron microscope project, J. Phys. Conf. Ser. 746 (2016) 012004, , https://doi.org/10.1088/1742-6596/746/1/012004.

[37] C. Carminati, P. Boillat, F. Schmid, P. Vontobel, J. Hovind, M. Morgano, M. Raventos, M. Siegwart, D. Mannes, C. Gruenzweig, P. Trtik, E. Lehmann, M. Strobl, A. Kaestner, Implementation and assessment of the black body bias correction in quantitative neutron imaging, PLOS ONE 14 (2019) e0210300, , https://doi.org/10.1371/journal.pone.0210300.